Supplementary Material for "Experimental realization of color-orbit coupling in an ultracold gas"

Chetan S. Madasu,[1,2] Chirantan Mitra,[1,2] Lucas Gabardos,[1,2] Ketan D. Rathod,[3,2,*] Thomas Zanon-Willette,[4] Christian Miniatura,[5,3] Frédéric Chevy,[6] Chang Chi Kwong,[1,2] and David Wilkowski[1,2,3,†]

[1] *Nanyang Quantum Hub, School of Physical and Mathematical Sciences, Nanyang Technological University, 21 Nanyang Link, Singapore 637371, Singapore*
[2] *MajuLab, International Joint Research Unit IRL 3654, CNRS, Université Côte d'Azur, Sorbonne Université, National University of Singapore, Nanyang Technological University, Singapore*
[3] *Centre for Quantum Technologies, National University of Singapore, 117543 Singapore, Singapore*
[4] *Sorbonne Université CNRS, MONARIS, UMR 8233, F-75005 Paris, France*
[5] *Université Côte d'Azur, CNRS, INPHYNI, 17 rue Julien Lauprêtre, 06200 Nice, France*
[6] *Laboratoire de Physique de l'École normale supérieure, ENS, Université PSL, CNRS, Sorbonne Université, Université de Paris, F-75005 Paris, France*

I. 2-TRIPOD LASER SYSTEM

The frequency difference of the σ^+ and σ^- beams is controlled by acousto-optic modulators (AOMs), as shown in Fig. 1b, at frequencies of -80 MHz and -80.0248 MHz, respectively. The 24.8 kHz frequency difference compensates for the shifts in the ground state Zeeman sublevels due to the bias magnetic field of 67 G (Landé factor -1.3×10^{-4}). We adjust the single-photon detuning to by at resonance with the right tripod with an upstream AOM [1]. We use the σ^+ and σ^- electro-optic modulators (EOMs) modulated at 14.12 MHz, where the -1 order sidebands target the σ^+ and σ^- transitions of the left tripod system. 14.12 MHz corresponds to the linear and quadratique Zeeman frequency shift difference between the excited states $\left|^3P_1, F = 9/2, m_F = 3/2\right\rangle$ and $\left|^3P_1, F = 9/2, m_F = 7/2\right\rangle$. Lastly, a laser beam controlled by a π-AOM at -94.132 MHz addresses the π transition in the left tripod system. The EOM in the π beam path is also modulated at 14.12 MHz so that the +1 order sideband targets the π transition of the right tripod. Here, the transition with the smallest Clebsch-Gordan coefficient is addressed with the carrier signal to minimize the modulation depth needed to equalize the Rabi frequencies. The modulation depths for the EOMs are given in table I. The carrier-to-first-sideband ratio values, shown in the second column, agree with the ratios of appropriate Clebsch-Gordan coefficients shown in the last column. With these modulation depths, we experimentally verify that

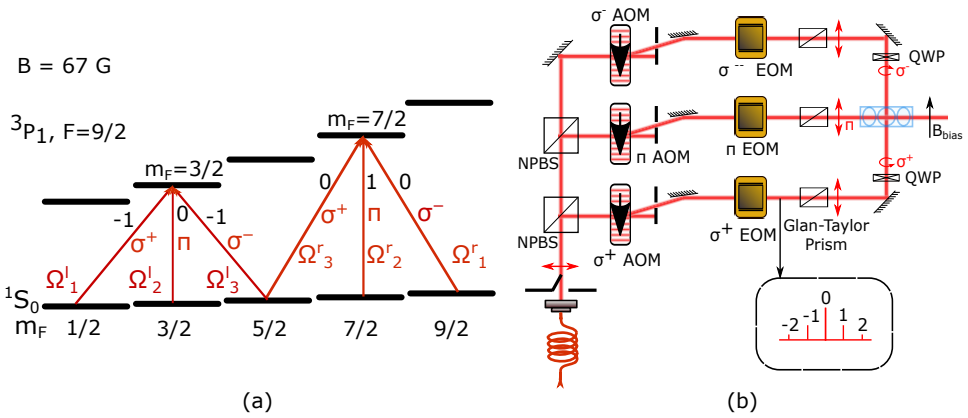

Figure 1. **Laser system** (a) Energy level scheme of 2-tripod configuration showing the sideband index and polarization of the laser beams. (b) Schematic showing the implementation of the 2-tripod scheme using AOMs and EOMs. Inset shows the schematic spectrum of light after EOM.

* Currently at Bennett University, Greater Noida 201310, India
† david.wilkowski@ntu.edu.sg

EOM	β	$\lvert J_1(\beta)/J_0(\beta)\rvert$
σ^+	1.28	$\sqrt{32/48}$
σ^-	1.10	$\sqrt{18/42}$
π	0.79	$\sqrt{9/49}$

Table I. The first column indicated the EOM referenced to the polarization of the laser. The second column shows the modulation depths necessary to achieve equal Rabi frequencies on transitions addressed with lasers with the same polarization. The $|J_1(\beta)/J_0(\beta)|$ ratios, shown in the third column, correspond to the Clebsch-Jordan coefficient ratios for transitions addressed with lasers with the same polarization.

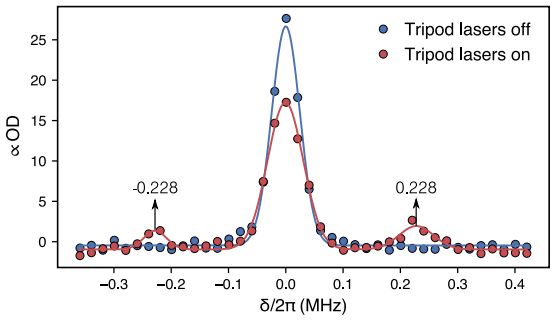

Figure 2. Dressed state spectroscopy of the $\left|{}^1S_0, F = 9/2, m_F = 5/2\right\rangle \rightarrow \left|{}^3P_1, F = 11/2, m_F = 7/2\right\rangle$ transition with (red symbols) and without (blue symbols) the excitation of 2-tripod lasers. When the 2-tripod lasers are on, we probe the dressed state energies. The two extra resonances at -228 kHz and 228 kHz are associated with the transitions from the dressed states $|B_3\rangle$ and $|B_4\rangle$, respectively. The resonances from the other dressed states $|B_1\rangle$ and $|B_2\rangle$ are not observed as $\langle B_1|5/2\rangle_g = \langle B_2|5/2\rangle_g = 0$.

the Rabi frequencies of the transitions are equal by performing Rabi oscillation on individual transitions. We also performed spectroscopy of $\left|{}^1S_0, F = 9/2, m_F = 5/2\right\rangle \rightarrow \left|{}^3P_1, F = 11/2, m_F = 7/2\right\rangle$ transition with and without the 2-tripod lasers to extract the frequency shift between the dressed states. Fig. 2 shows that the extreme bright states ($|B_3\rangle$ and $|B_4\rangle$ as defined in Fig. 1b of the main text) are shifted equally from the center peak by the Rabi frequency of our tripod beams. We note that the two other bright states ($|B_1\rangle$ and $|B_2\rangle$) remain unpopulated, explaining why sidebands at $\Omega/\sqrt{2}$ are not visible in Fig. 2 (see ref. [1] for more details).

Importantly, the remaining sidebands, generated by the EOMs, are addressing (quasi-) resonantly other transitions not connected to the 2-tripod scheme. Hence, they only contribute to residual AC-stark shift that is estimated to be below the recoil energy.

The tripod AOMs are powered by amplified RF signals from an Analog Devices AD9852 Direct Digital Synthesizer (DDS) to control the laser detuning. The tripod EOMs are driven by Rigol DG4102 function generators and amplified by RF amplifiers, which can be triggered during the tripod laser sequence. The total beam power is managed by adjusting the RF power supplied to the AOMs, while the sideband distribution is controlled by changing the RF power to the EOMs, which modifies the modulation depth.

II. COLOR-ORBIT COUPLING HAMILTONIAN

The three degenerate dark-states of the 2-tripod scheme for the orientation of the laser beams shown in Fig. 1b can be chosen as [2]

$$
\begin{aligned}
|D_l\rangle =& \sin\varphi_l e^{4iky - i(\delta_1^l - \delta_3^l)t}\,|9/2\rangle_g - \cos\varphi_l e^{ik(-x+3y) - i(\delta_2^l - \delta_3^l)t}\,|7/2\rangle_g \\
|D_0\rangle =& \frac{1}{\alpha_0}[\cot\vartheta_l(\cos\varphi_l e^{4iky - i(\delta_1^l - \delta_3^l)t}\,|9/2\rangle_g + \sin\varphi_l e^{ik(-x+3y) - i(\delta_2^l - \delta_3^l)t}\,|7/2\rangle_g) - e^{2iky}\,|5/2\rangle_g + \\
& \cot\vartheta_r(\sin\varphi_r e^{ik(-x+y) - i(\delta_2^r - \delta_3^r)t}\,|3/2\rangle_g + \cos\varphi_r e^{-i(\delta_1^r - \delta_3^r)t}\,|1/2\rangle_g)] \\
|D_r\rangle =& \sin\varphi_r e^{-i(\delta_1^r - \delta_3^r)t}\,|1/2\rangle_g - \cos\varphi_r e^{ik(-x+y) - i(\delta_2^r - \delta_3^r)t}\,|3/2\rangle_g
\end{aligned}
\tag{1}
$$

where $\varphi_a = \arctan\left(\frac{|\Omega_2^a|}{|\Omega_1^a|}\right)$, $\vartheta_a = \arccos\left(\frac{|\Omega_3^a|}{\sqrt{|\Omega_1^a|^2+|\Omega_2^a|^2+|\Omega_3^a|^2}}\right)$ for $a = \{l, r\}$ corresponding respectively to left and right tripod lasers and $\alpha_0 = \sqrt{1+\cot^2\vartheta_l+\cot^2\vartheta_r}$. Here Ω_i^a are the Rabi-frequencies and δ_i^a are the detunings of the double tripod lasers, with $i = \{1, 2, 3\}$. Using the dark-states basis in Eqs. 1, the terms of the Hamiltonian

$$\hat{H} = \frac{\hat{\mathbf{p}}^2}{2m} - \frac{\hat{\mathbf{p}}\cdot\hat{\mathbf{A}}}{m} + \hat{W} + \hat{\Delta} \tag{2}$$

read,

$$\begin{aligned}\hat{\mathbf{A}} =& \hbar k \begin{pmatrix} \cos^2\varphi_l & -\cot\vartheta_l \sin 2\varphi_l/2\alpha_0 & 0 \\ -\cot\vartheta_l \sin 2\varphi_l/2\alpha_0 & (\cot^2\vartheta_l \sin^2\varphi_l + \cot^2\vartheta_r \sin^2\varphi_r)/\alpha_0^2 & -\cot\vartheta_r \sin 2\varphi_r/2\alpha_0 \\ 0 & -\cot\vartheta_r \sin 2\varphi_r/2\alpha_0 & \cos^2\varphi_r \end{pmatrix} \hat{\boldsymbol{e}}_x - \\ & \hbar k \begin{pmatrix} (3+\sin^2\varphi_l) & \cot\vartheta_l \sin 2\varphi_l/2\alpha_0 & 0 \\ \cot\vartheta_l \sin 2\varphi_l/2\alpha_0 & (\cot^2\vartheta_l(3+\cos^2\varphi_l) + \cot^2\vartheta_r \sin^2\varphi_r + 2)/\alpha_0^2 & -\cot\vartheta_r \sin 2\varphi_r/2\alpha_0 \\ 0 & -\cot\vartheta_r \sin 2\varphi_r/2\alpha_0 & \cos^2\varphi_r \end{pmatrix} \hat{\boldsymbol{e}}_y \end{aligned} \tag{3}$$

$$\hat{W} = -\frac{\hbar^2 k^2}{m} \begin{pmatrix} (5+3\sin^2\varphi_l) & 3\cot\vartheta_l \sin 2\varphi_l/2\alpha_0 & 0 \\ 3\cot\vartheta_l \sin 2\varphi_l/2\alpha_0 & (\cot^2\vartheta_l(5+3\cos^2\varphi_l) + \cot^2\vartheta_r \sin^2\varphi_r + 2)/\alpha_0^2 & -\cot\vartheta_r \sin 2\varphi_r/2\alpha_0 \\ 0 & -\cot\vartheta_r \sin 2\varphi_r/2\alpha_0 & \cos^2\varphi_r \end{pmatrix} \tag{4}$$

$$\begin{aligned}\hat{\Delta} =& -\hbar \begin{pmatrix} \delta_1^l \sin^2\varphi_l + \delta_2^l \cos^2\varphi_l - \delta_3^l & \frac{1}{2\alpha_0}\left(\cot\vartheta_l \sin 2\varphi_l(\delta_1^l - \delta_2^l)\right) & 0 \\ \frac{1}{2\alpha_0}\left(\cot\vartheta_l \sin 2\varphi_l(\delta_1^l - \delta_2^l)\right) & \frac{1}{\alpha_0^2}\sum_{a=\{l,r\}} \cot^2\vartheta_a(\delta_2^a \sin^2\varphi_a + \delta_1^a \cos^2\varphi_a - \delta_3^a) & \frac{1}{2\alpha_0}\left(\cot\vartheta_r \sin 2\varphi_r(\delta_1^r - \delta_2^r)\right) \\ 0 & \frac{1}{2\alpha_0}\left(\cot\vartheta_r \sin 2\varphi_r(\delta_1^r - \delta_2^r)\right) & \delta_1^r \sin^2\varphi_r + \delta_2^r \cos^2\varphi_r - \delta_3^r \end{pmatrix} \\ & - \frac{i\hbar}{\alpha_0} \begin{pmatrix} 0 & -\cot\vartheta_l \frac{\partial\varphi_l}{\partial t} & 0 \\ \cot\vartheta_l \frac{\partial\varphi_l}{\partial t} & 0 & \cot\vartheta_r \frac{\partial\varphi_r}{\partial t} \\ 0 & -\cot\vartheta_r \frac{\partial\varphi_r}{\partial t} & 0 \end{pmatrix} \end{aligned} \tag{5}$$

We note that $\varphi_a = 0$ once the tripod beams are turned on. Hence, $\hat{\Delta} \neq 0$ if $\delta_i^a \neq 0$, meaning that the detunings can be used to engineer an extra scalar potential. In addition, the geometric scalar potential $\hat{W}$ depends on the orientation of tripod lasers and has of the same order of magnitude as $\langle\hat{\mathbf{p}}\cdot\hat{\mathbf{A}}\rangle/m$ when $|\langle\hat{\mathbf{p}}\rangle| \approx \hbar k$. Hence, the detunings remain moderated to obtain a $\hat{\Delta}$ term in the same order of magnitude as the $\hat{W}$ term. Fig. 3a shows the energy branches for equal Rabi frequencies of the 2-tripod lasers in the presence of the geometric scalar potential. This scalar field breaks the degeneracy between the dark states when the tripod lasers satisfy the two-photon resonance condition ($\delta_i^a = 0$). Since the transfer of population among the bare states is coherent, it goes with a deterministic change in velocity giving rise to Doppler-induced frequency shift. For example, an atom in $|9/2\rangle_g$ acquires a velocity of $2v_r\hat{\boldsymbol{e}}_y$ when it is transfered into $|5/2\rangle_g$ due to photon redistribution. $v_r = \hbar k/m$ is the recoil velocity. Therefore, the transitions coupling $|5/2\rangle_g$ namely, $|5/2\rangle_g \to |7/2\rangle_e$ is blue shifted by $2\hbar k^2/m = 4\omega_r$ and $|5/2\rangle_g \to |3/2\rangle_e$ is red shifted by $4\omega_r$ where $\omega_r = \hbar k^2/2m = 2\pi \times 4.795$ kHz is the recoil frequency. These shifts can be compensated by detuning the 2-tripod lasers as shown in the table II. By compensating for these shifts, we bring all the 2-tripod transitions at resonance for an atom at rest. We get the color-orbit Hamiltonian, depicted in Eq. (2) of the main text after the scalar potential cancellation (namely $\hat{\Delta} = -\hat{W}$). The Fig. 3b shows the resulting energy dispersion of the system.

δ_1^l	δ_2^l	δ_3^l	δ_3^r	δ_2^r	δ_1^r
-8ω_r	-2ω_r	4ω_r	-4ω_r	-2ω_r	0

Table II. Detunings of the 2-tripod lasers that result in the cancellation of SU(3) scalar potential.

Using the dark-states basis defined in Eq. 1, we compute the color basis, used in the main text, as follows:

$$\begin{aligned} |R\rangle &= \frac{1}{\sqrt{2}}(|D_0\rangle - e^{i\pi/4}|D_r\rangle) \\ |G\rangle &= \frac{1}{\sqrt{2}}(|D_0\rangle + e^{i\pi/4}|D_r\rangle) \\ |B\rangle &= |D_l\rangle\,. \end{aligned} \tag{6}$$

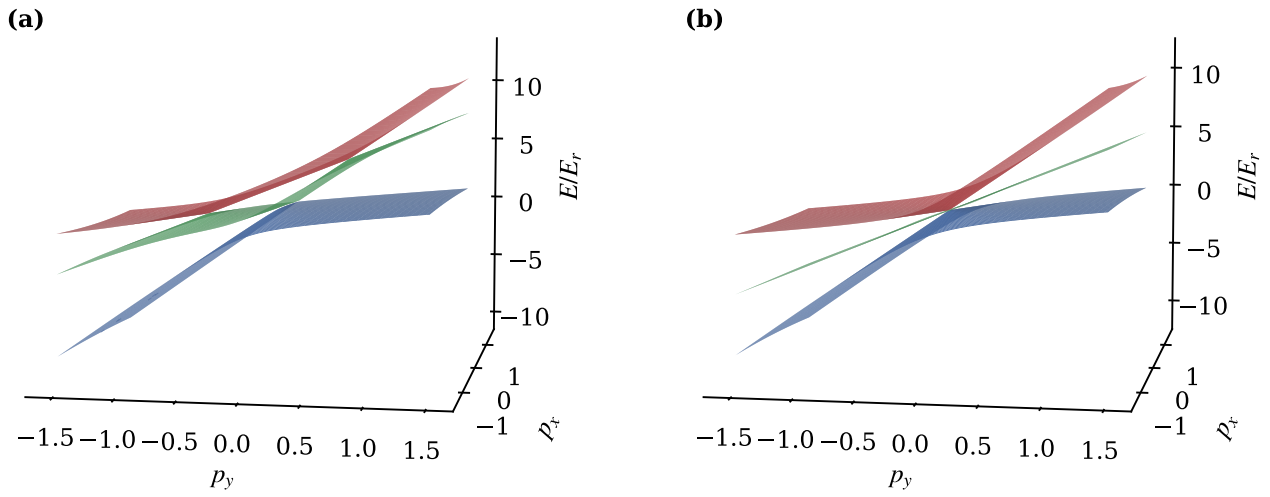

Figure 3. **Effect of the scalar potential**. Energy branches obtained by diagonalization of the Hamiltonian in Eq. (2) for equal Rabi frequencies of the 2-tripod lasers in the presence **(a)** and absence **(b)** of the geometric scalar potential.

The matrices in Eqs. (3-5) are computed in the color basis by using the relationship $\hat{M}_{\text{color}} = \hat{B}^{\dagger}\hat{M}_{\text{dark}}\hat{B}$ where the change of basis matrix $\hat{B}$ reads,

$$\hat{B} = \frac{1}{\sqrt{2}} \begin{pmatrix} 0 & 0 & \sqrt{2} \\ 1 & 1 & 0 \\ -e^{i\pi/4} & e^{i\pi/4} & 0 \end{pmatrix}, \tag{7}$$

$\hat{M}_{\text{color}}$ is any matrix in the color basis and $\hat{M}_{\text{dark}}$ the corresponding matrix in the dark-state basis.

III. INITIAL STATE PREPARATIONS

Color-orbit coupling: Prior to the system evolving under the color-orbit Hamiltonian, we adiabatically prepare the atoms into the dark-states subspace. After optical pumping, we have prepared atoms in $|9/2\rangle_g$. Then, we turn on the σ^+ and π beams along with their sidebands abruptly and ramp the power of σ^- laser as a function of time such that $\Omega_3^l(t) = \Omega_1^r(t) = \Omega \tan\left(\frac{\pi t}{4t_{\text{ramp}}}\right)$, where $t \leq t_{\text{ramp}}$. t_{ramp} is the duration of the ramp and $\Omega = 2\pi \times 228$ kHz is the Rabi frequency of all the transitions in the 2-tripod. The function for ramping the Rabi frequencies is chosen such that the second term of the detuning matrix in Eq. 5 is constant during the ramp. In the experiments presented in the main text, $t_{\text{ramp}} = 18\mu$s. As the Hamiltonian during the ramp is dependent on time and momentum, the state after the ramp is also depending of the duration of the ramp and the detunings. Fig. 4 shows the populations of the dark states after ramping the Rabi frequencies with a momentum kick of $4\hbar k$ as a function of a kick's angle θ with respect to the x-axis.

Cartan-Weyl transformation For the experimental data depicted in Fig. 2 in the main text, the initial state $|G\rangle$ is prepared using identical ramps for the Rabi frequencies as discussed above, but with additional detunings of $\delta_3^r = 2\delta_2^r = 50$ kHz.

The state in the dark-state basis (and further in the color basis) is reconstructed from the bare state populations extracted from time-of-flight images. For equal Rabi-frequencies, the parameters of the state in the dark state basis $|\psi\rangle = d_l e^{i\alpha}|D_l\rangle + d_0|D_0\rangle + d_r e^{i\beta}|D_r\rangle$ read,

$$
\begin{aligned}
d_l &= \sqrt{p_{1/2} + p_{3/2} - \frac{p_{5/2}}{2}} \\
d_0 &= \sqrt{2p_{5/2}} \\
d_r &= \sqrt{p_{7/2} + p_{9/2} - \frac{p_{5/2}}{2}} \\
\alpha &= \cos^{-1}\left(\frac{p_{1/2} - p_{3/2}}{d_0 d_l}\right) \\
\beta &= \cos^{-1}\left(\frac{p_{9/2} - p_{7/2}}{d_0 d_r}\right)
\end{aligned}
\tag{8}
$$

where p_{m_F} is the population of the ground state $|m_F\rangle_g$. Hence, a dressed state is reconstructed to an irrelevant global phase, under the adiabatic subsumption that the bright states remain unpopulated. We note that the signs of the two remaining phases α and β are unknown and extracted with the help of a numerical integration.

IV. CORRECTION OF EXPERIMENTAL BIAS

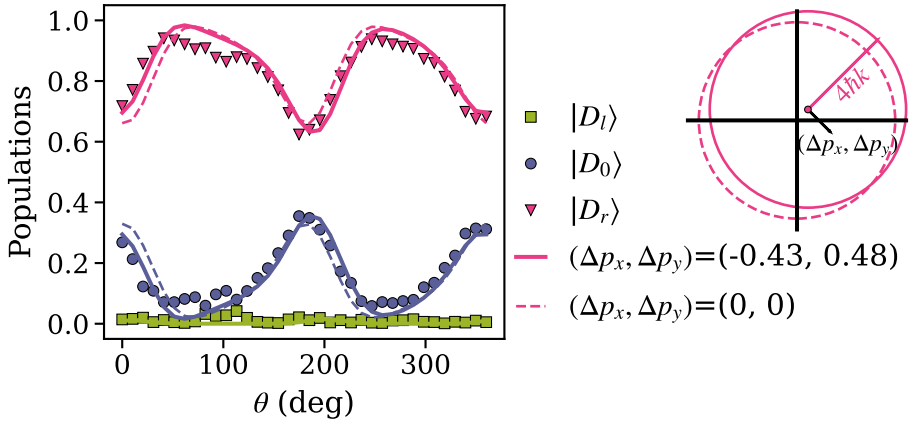

Figure 4. **Characterization of the Initial State**. Populations of the dark states after the state preparation ramps with a momentum kick of $4\hbar k$ as a function of the kick's angle θ. Dashed lines are the expected populations found by numerical integration of the Schrödinger equation. Plain lines are obtained by fitting the experimental data with the numerical solution with center of momentum space $(\Delta p_x, \Delta p_y)$ as the free parameters.

As the strength of the gauge field in Eq. (3) is of the order of recoil momentum $\hbar k$, and the scalar potential and the detuning matrix are of the order of recoil energy $\hbar^2 k^2/(2m)$, our experimental results are sensitive to the biases of similar order of magnitude. Possible biases are off-resonant coupling outside the 2-tripod scheme, AC-stark shifts caused by the spectator sidebands created by the EOMs, and non-zero mean momentum kick during the preparation of the gas. In this section, we qualitatively discuss the cumulative effect of these biases on the experimental data.

Fig. 4 shows the populations of the dark states after ramping the Rabi frequencies with a momentum-kick amplitude of $4\hbar k$ as a function of the kick's angle θ with respect to the x-axis. Within the relatively short duration of the state preparation, we notice that there is a mismatch with the numerical results (dashed lines). We recast the frequency biases in the experimental system to an effective initial momentum. The latter corresponds to a residual detuning matrix. Then, we fit the experimental data using a numerical integration where the initial momentum is taken as the free parameter. The fit indicates that the mismatch with the experimental data can be minimized for an initial momentum $(p_x, p_y) = (-0.43\hbar k, 0.48\hbar k)$.

Even though the correction is only at the percent level of the initial momentum, we find a substantial improvement between the numerical integration and the experiment for the color-orbit interaction dynamics discussed in the main text. Fig. 5a shows the bare state populations as a function of time. The plain (dashed) lines are the numerical results with (without) the addition of the initial momentum correction discussed above. Fig. 5b shows the population

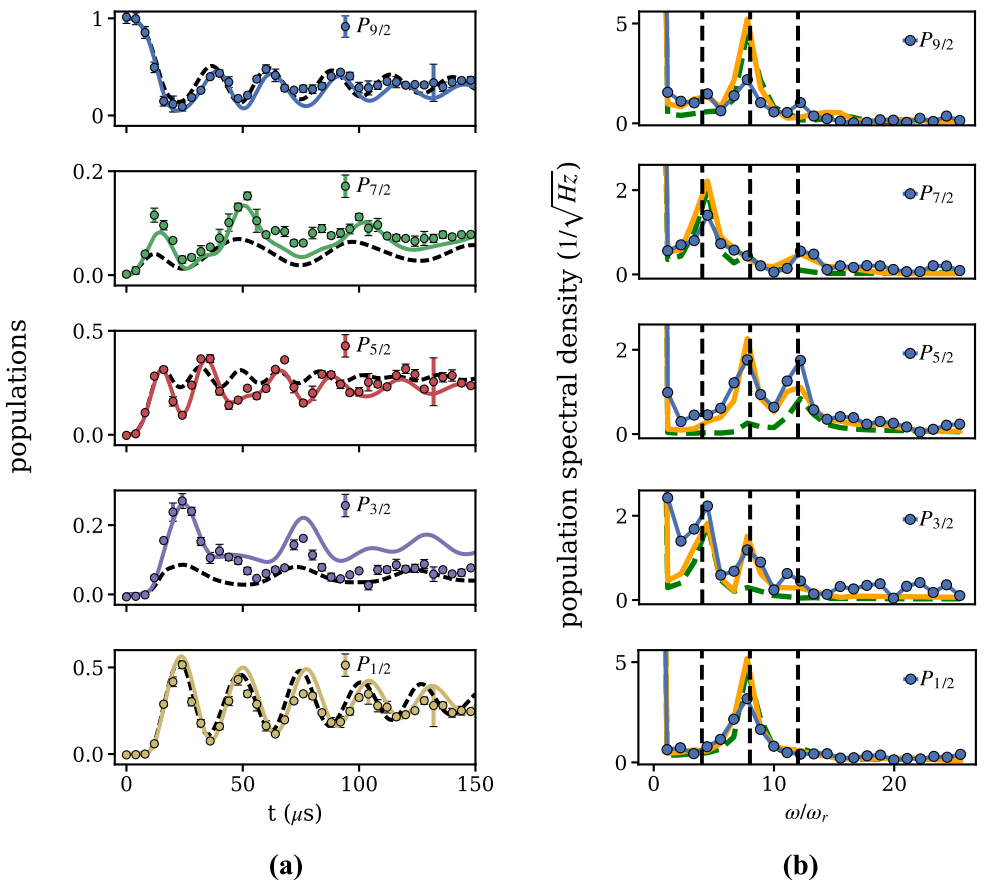

Figure 5. **Color-orbit coupling with and without momentum correction: First example**. **(a)** Evolution bare state populations of atoms initially in $|9/2\rangle_g$ under the color-orbit coupling Hamiltonian with a momentum kick of $8\hbar k\hat{\boldsymbol{e}}_x$. **(b)** Spectra of the bare state populations. Colored-plain (dashed-black) curves are the numerical results with (without) the initial momentum correction.

spectral density (Fig. 3c of the main manuscript) along with the corrected spectra (orange plain lines). Here, the positions of the resonances are robust, but their amplitudes are in better agreement with the simulation considering the initial momentum correction.

To highlight the general character of the correction, we prepare another initial state to check if the correction, found previously, still improves the agreement between the experiment and the simulation. Here, we transfer the population of $|9/2\rangle_g$ to $|5/2\rangle_g$ using a STIRAP pulse sequence. We prepare the new initial state by abruptly turn on π beams and slowly ramp the σ^+ and σ^- beams as the same function of time as in the above case, i.e. $\Omega_1^l(t) = \Omega_3^l(t) = \Omega_3^r(t) = \Omega_1^r(t) = \Omega_0 \tan\left(\frac{\pi t}{4t_{\text{ramp}}}\right)$. This ramping sequence is symmetric by interchanging the left and right tripod, so the bare state populations of $|9/2\rangle_g$ and $|7/2\rangle_g$ is expected to be equal to $|1/2\rangle_g$ and $|3/2\rangle_g$, respectively. This symmetry is reflected in the dashed-black curves in Fig. 5a corresponding to the numerical integration without the correction. However, this symmetry is broken for the bare-state population data (circles). This is also true for the numerical integration corrected for the initial momentum (plane lines). The latter is now in good agreement with the experimental data. The data depicted in Fig. 5a were taken with a momentum kick of $8\hbar k\hat{\boldsymbol{e}}_x$. If we now consider a momentum kick with an opposite sign, namely of -$8\hbar k\hat{\boldsymbol{e}}_x$, we effectively interchange the left and right tripod. This point can be checked on the plain curves of Fig. 5b corresponding to the numerical integration with correction. Again, we observe a better agreement with the experimental data (circles) than for the uncorrected numerical integration (dashed-black curves).

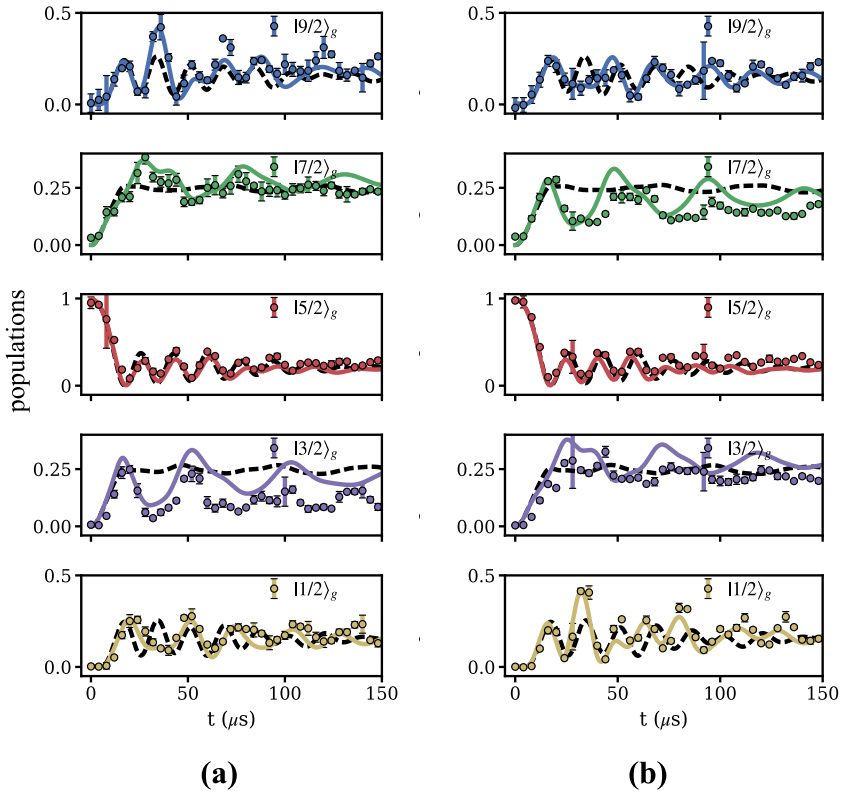

Figure 6. **Color-orbit coupling with and without momentum correction: Second example**. Evolution of bare state populations of the atoms initially in $|5/2\rangle_g$ under the color-orbit coupling Hamiltonian with a momentum kick of $8\hbar k\hat{\boldsymbol{e}}_x$ **(a)** and -$8\hbar k\hat{\boldsymbol{e}}_x$ **(b)**. Colored-plain (dashed-black) curves are the numerical results with (without) the initial momentum correction.

V. GELL-MANN MATRICES AND CARTAN-WEYL LADDER MATRICES

The Gell-Mann matrices from a representation of the Lie algebra of the SU(3) group [3]. They read

$$\hat{\lambda}_1 = \begin{bmatrix} 0 & 1 & 0 \\ 1 & 0 & 0 \\ 0 & 0 & 0 \end{bmatrix} \quad \hat{\lambda}_2 = \begin{bmatrix} 0 & -\mathrm{i} & 0 \\ \mathrm{i} & 0 & 0 \\ 0 & 0 & 0 \end{bmatrix}$$
$$\hat{\lambda}_3 = \begin{bmatrix} 1 & 0 & 0 \\ 0 & -1 & 0 \\ 0 & 0 & 0 \end{bmatrix} \quad \hat{\lambda}_4 = \begin{bmatrix} 0 & 0 & 1 \\ 0 & 0 & 0 \\ 1 & 0 & 0 \end{bmatrix}$$
$$\hat{\lambda}_5 = \begin{bmatrix} 0 & 0 & -\mathrm{i} \\ 0 & 0 & 0 \\ \mathrm{i} & 0 & 0 \end{bmatrix} \quad \hat{\lambda}_6 = \begin{bmatrix} 0 & 0 & 0 \\ 0 & 0 & 1 \\ 0 & 1 & 0 \end{bmatrix}$$
$$\hat{\lambda}_7 = \begin{bmatrix} 0 & 0 & 0 \\ 0 & 0 & -\mathrm{i} \\ 0 & \mathrm{i} & 0 \end{bmatrix} \quad \hat{\lambda}_8 = \frac{1}{\sqrt{3}} \begin{bmatrix} 1 & 0 & 0 \\ 0 & 1 & 0 \\ 0 & 0 & -2 \end{bmatrix}. \tag{9}$$

The Cartan-Weyl raising and lowering operators are defined as,

$$\hat{T}_\pm = \frac{1}{2}\left(\hat{\lambda}_1 \pm i\hat{\lambda}_2\right), \quad \hat{V}_\pm = \frac{1}{2}\left(\hat{\lambda}_4 \pm i\hat{\lambda}_5\right), \quad \hat{U}_\pm = \frac{1}{2}\left(\hat{\lambda}_6 \pm i\hat{\lambda}_7\right). \tag{10}$$

[1] C. S. Madasu, *Experimental investigation of non-Abelian artificial gauge fields: from SU(2) to SU(3)*, Ph.D. thesis, Nanyang Technological University (2023).
[2] Y.-X. Hu, C. Miniatura, D. Wilkowski, and B. Grémaud, U (3) artificial gauge fields for cold atoms, Physical Review A **90**, 023601 (2014).
[3] H. Georgi, *Lie Algebras in Particle Physics (2nd ed.)* (Westview Press, 1999).